Effects of cryogenic temperature and pre-stretching on mechanical properties and deformation characteristics of a peak-aged AA6082 extrusion

Zebing Xu [a], Hans J. Roven [a,*], Zhihong Jia [b]

[a] Department of Materials Science and Engineering, Norwegian University of Science and Technology, 7491 Trondheim, Norway

[b] College of Materials Science and Engineering, Chongqing University, 400044, China

* Corresponding author at: **Department of Materials Science and Engineering,**

NTNU, Norwegian University of Science and Technology, 7491 Trondheim, Norway

E-mail: hans.j.roven@ntnu.no

Abstract

Plastic deformation and surface characteristics of a peak-aged AA6082 alloy have been studied by means of tensile tests, Scanning Electron Microscopy (SEM), Electron Backscatter Diffraction (EBSD), Transmission Electron Microscopy (TEM) and Atom force Microscopy (AFM). The results showed that a simultaneous enhancement in ductility and strength of the alloy was obtained at 77K in comparison with that at 295K. The enhanced properties at 77K are attributed to higher work hardening accompanied by a more homogeneous slip mode. Moreover, in order to clarify the effect of temperature-induced microstructural changes on mechanical properties, a further investigation, i.e., pre-stretching at 77K and 295K with or without subsequent annealing treatment, followed by tension to fracture at 295K, was conducted. It was found that pre-stretching at both temperatures produce a yield point and followed by different yield drop zones, while pre-stretching and annealing lead to reduced stress levels, much less pronounced yield point behavior and improved ductility compared to their predecessors. Especially, pre-straining at 77K with subsequent annealing demonstrated the highest ductility and work hardening ability among the four cases. It is thought the obtained

results are associated with variety of microstructure such as strain localization, β'/β" ratio and dislocation densities under different conditions.

Keywords: AA6082 alloy; cryogenic temperature; mechanical property; Pre-stretching; homogenous deformation

1 Introduction

Due to attractive mechanical properties such as moderate to high strength, good weld ability and high corrosion resistance, aluminum AA6000 series alloys have attracted considerable attention during the last decades. In industrial application, two-thirds of all extruded product are made of aluminum and 90% of those are made from 6000 series alloys [1]. In this series, AA6082 alloy is one of the most widely used alloys [2-5]. These materials can be heat treated to produce precipitation to various degree, the peak ageing treatment involving solution heat treatment with aim of obtaining supersaturated α solid solution and subsequent artificial ageing so as to accelerate the changes in the properties of an alloy as a result of precipitation hardening, is a common method to increase the strength of the alloy [6]. More specifically, the strength is determined by the structure of the precipitates and in particular the degree of coherency with the Al matrix [7]. The establishment of accurate relationships between plastic behavior, process parameters and chemical elements has been done in many excellent works to demonstrate intrinsic features of these alloys and their industrial applications [8]. However, demanding new applications rely on continuous research and development. Here, the relationships between mechanical properties, deformation behavior, microstructure, processing parameters as well as working conditions are of particular importance.

It is well know that the mechanical properties of materials are among the most important physical properties that determine the range of possible applications. Mechanical properties are mainly dependent on the composition, phase structures and defects, and the properties change as function of temperature. It has been reported that materials often have some undesirable or unusual properties at cryogenic temperatures, and which make them attractive to cryogenic engineering such as liquefied natural gas (LNG) tank [9]. In the last decades, a number of research works have been carried out to clarify the cryogenic temperature - mechanical properties - microstructure evolution relations of pure Al and its alloys. For example, measurements of the dislocation density in pure Al alloys at 4.2K, suggested that failure upon loading of these materials occurs when the local dislocation density approaches the critical value for spontaneous annihilation [10]. In a study involving Al-Li alloys with various lithium additions, the authors reported that the nature of dispersed particles had significant influence on the mechanism of plastic deformation in the temperature region 40-170K [11]. In another study on the work hardening behavior versus deformation temperature for pure Al [12], the authors concluded that suppression of dynamic recovery during deformation at low temperature preserved a high density of dislocations, i.e. simultaneously improving strength and elongation to fracture. Further, for an AA5754 alloy, one reported that crystallographic texture formed at lower temperature was weaker than that produced at higher temperature, e.g. after the same strain. Consistently, the lattice rotations were suppressed as the deformation temperature declined [13]. Such studies indicate that design of new test procedures and methodologies for Al- alloys at cryogenic temperature are becoming more and more interesting, i.e. since the material properties and microstructure improve and change significantly during deformation at cryogenic temperature.

In addition to the changes in mechanical properties and texture evolution at cryogenic temperatures, the surface roughness might develop otherwise than at room temperature.

Generally, the deformation mechanisms that generate surface roughening are governed by the following three principal reasons [14]: (1) the surface grains are less constrained than interior grains and thus deform more easily; (2) the free surface allows formation of surface reliefs; (3) strain concentration around a defect or an inclusion is highest at the free surface. As a result, the surface roughening behavior becomes a factor that not only determines the quality of the material, but can also be a measure of the suitability of a particular alloy for a given application. For this reason, basic studies that relate metallurgical factors for a particular alloy to a performance requirement parameter, such as surface roughness, are needed to develop better predictions of surface appearance, ductility of material, etc. To the best of the present author's knowledge, such studies on the cryogenic behavior of AA6082 alloys have not been sufficiently explored. Therefore, the present work involves systematic studies on plasticity of an AA6082 alloy conducted at 77K and 295K, aiming to characterize mechanical properties and to identify processes that control plastic flow, strain hardening behavior and deformed surface characteristics. Especially, the mechanical properties of pre-stretched samples at 77K and 295K are compared and an observed yield drop phenomenon is presented and discussed. Hence, the present work provides new information on the cryogenic behavior of this type of non-recrystallized alloys.

2 Experiment procedures

The material used in this investigation was an AA6082 alloy supplied by Hydro Aluminum having the chemical composition (in wt%): 1.005Si, 0.165Fe, 0.497Mn, 0.687Mg, 0.01Zn, and Al balance. The as-received (AS) material was in the form of an extrusion plate, 10 mm thick. A subsequent heat treatment put the billet into peak-aged condition (T6 temper), and then rectangular tensile specimens having 2mm thickness were machined from the plate mid-section of aged material, e.g. with the tensile axis being parallel to the extrusion direction

(ED) and the specimen width in the normal direction (ND), as shown in Fig.1. The gauge section of these specimens was 32mm and 6mm, e.g. in length and width respectively. The top surface of all peak-aged samples were then grinded and polished using standard metallographic techniques, followed by electro-chemical polishing (solution of 80% C_2H_5OH + 20% $HCLO_4$, 20V, 1,5A, -30°C and 15s) to minimize possible effects from the machined surface layers. Tensile tests were then conducted in a universal servo-hydraulic test machine (MTS880) at an initial strain rate of $10^{-4}s^{-1}$ at 77K and 295K. Three specimens were used for each temperature. The cryogenic tests were performed by submerging the samples and grips into liquid nitrogen in an in-house fixture mounted to the testing machine. Before testing, the specimens were kept for 15 minutes in order to achieve thermal equilibrium between the cryogenic liquid and the specimen. Furthermore, tensile strain was calculated from the registered cross-head displacement after subtraction of the machine compliance.

In addition to the peak aged specimens tensioned to fracture directly, 6 specimens were pre-strained to 10% at 295K and 6 specimens were pre-strained to 10% at 77K. Then 3 samples from each pre-straining temperature were stored at room temperature for 5 days and finally tensioned to fracture at room temperature. In addition, the remaining 6 pre-strained samples were annealed at 160°C for 5 hours before being subjected to a full tensile test at room temperature. In this study, pre-stretching procedure was used to create different characteristic substructure morphologies in the samples. The samples which have been pre-stretched at liquid nitrogen and pre-stretching at room temperature were labeled as PSL and PSR samples, respectively. Same as that for specimens tensioned to fracture, the strain rate of 10^{-4} s^{-1} was set in order to stabilize temperature during tension. The subsequent annealing treatment, where the annealing temperature was much lower than the ageing temperature for 6000 series alloy, was conducted to reduce the dislocation density but without significantly changing the microstructure in terms of grain orientations and precipitate structures. The annealed specimens

were referred to as "pre-stretching in liquid nitrogen and annealing" (PSLA) and "pre-stretching at room temperature and annealing" (PSRA), respectively. For more clarity of the procedure, please refer to the schematic flow illustration in Fig. 2.

Moreover, three-dimensional (3-D) surface topography inspections of pre-stretched specimens (PSL and PSR samples) were acquired with an atomic force microscope (AFM, MultiMode 8) operated at room temperature in the contact mode. These measurements were carried out on the plane defined by the extrusion and normal directions (see Fig. 1). Subsequently, EBSD analysis was performed on the same plane of the stretched specimens in a Hitachi SU-6600 field emission gun SEM (FEG-SEM) equipped with a Nordif EBSD detector and TSL OIM software, large areas of about 1.2 mm^2 and step size of 1 μm were used. Finally, the dislocation substructures of fractured specimens were observed using a Libra200 transmission electron microscope (TEM), in accordance to the procedures described in a previous work [15]

3 Results and discussion

3.1 Microstructure of as-received material

Orientation imaging microscopy (OIM), i.e. using the electron backscattered diffraction (EBSD) technique, was applied to reveal the overall microstructure of the starting material in peak-aged condition (see Fig. 3). The shown micrographs are taken in the ED-ND plane. Here, black and white lines in the EBSD map of Fig. 3a, indicate locations of high grain boundaries (⩾15°, dark lines) and low angle grain boundaries (2-15°, white lines), respectively. The different color contrasts in the EBSD maps correspond to the different grain orientations, here, showing lamellar grains lying parallel to the extrusion axis. The present alloy contains Mn and Fe, which form high temperature stable dispersoids that prevent recrystallization. Hence the thermo-mechanically processed material forms a deformed fibrous grain structure. The corresponding orientation distribution functions (ODF) obtained from EBSD mapping shows

that the crystallographic texture is dominated by a strong cube (maximum intensity 30.7) accompanied by a minor Goss component.

Back scattered electron (BSE) imaging is typically used to provide information of distribution of particles having relatively high atomic number. Mn-rich dispersiods and fragmented primary constituent particles are shown in Fig. 4a, these particles are larger than the dispersoids being spherical or short-rod-like. A constituent particle has been marked (Fig. 4a) and the corresponding EDS analysis is shown in Fig. 4b. This particle contains Al, Fe, Mn and Si and is therefore a primary phase originated from the casting process. Such particles may reduce ductility when they are not fragmented and relatively small in size. If they have a size of the order of 1-5 μm, they can stimulate recrystallization by the particle stimulated nucleation (PSN) mechanism.[16]. On the other hand, the dispersoids hinder grain boundary movements and therefore restrict recovery and recrystallization upon the hot extrusion process [17]. The resulting grain structure is therefore fibrous, i.e. elongated and partly non-recrystallized (see Fig. 3). In the peak-aged condition, a large part of the strength is due to the hardening β" precipitates. A few of them are shown in approximate edge-on view along the [100] direction at high magnification in Fig. 4c and at a slightly lower magnification having a longitudal view in Fig. 4d. To be noted is the precipitate free zone (PFZs) seen in Fig. 4d. The zone is approximately 50 nm wide, and represents a soft area which is prone to localize plastic strain and reduce ductility [18, 19].

3.2 Mechanical properties and fracture characteristics

Fig. 5a shows the engineering stress-strain curves of peak-aged AA6082 alloy tensioned to fracture at 77K and 295K. The corresponding mechanical properties are listed in Table 1. It is clearly seen that the mechanical properties exhibit a significant improvement at 77K compared with those at 295K, e.g. an increase in yield strength from of 326 to 403 MPa, ultimate tensile strength from 377 to 492 MPa, and a ductility improvement from 15.6% to

18.5%. The variations in strength and ductility are closely related to the work hardening behavior, i.e. being influenced by the testing temperature in the present case. To characterize the work hardening behavior, the nominal stress-strain data were firstly transformed to true stress-strain data (σ is the true stress and ε is the true strain) and then plotted as $d\sigma/d\varepsilon$ *vs.* ε. The results are given in Fig. 5b, where the true stress and work hardening rate are presented as a function of true strain. As well known, failure occurs when a critical stress or strain is reached. In general, failure is normally trigged by the geometric instability that occurs when the work hardening rate $d\sigma/d\varepsilon$ drops below the corresponding true stress (i.e. the onset of necking). However, with the calculation results shown in Fig. 5b, the onset of necking occurring at the uniform strain (e_u), appears to happen differently at 77K and 295K. At the latter test temperature, onset of necking is premature with regard to the instability criteria, i.e. occurring at σ significantly less than $d\sigma/d\varepsilon$. However, at 77K the onset of necking is more or less fulfilling the criteria $d\sigma/d\varepsilon = \sigma$ (see the curves for 77K in Fig. 5b). Therefore, onset of necking in this alloy in the peak-aged condition is more likely to be dominated by premature local instabilities at 295K, but by macroscopic geometric instabilities at 77K. This indicates that a more homogeneous deformation is achieved at 77K than at 295K. In other words, an increased work hardening rate and thus the improved uniform elongation at cryogenic temperature could be considered as a consequence of such homogeneous deformation. More details on the deformation mechanisms versus temperature can be obtained from the TEM micrographs in Fig. 6, i.e. through comparing the dislocation slip behavior in the regions adjacent to the tensile fracture surfaces. For the specimen deformed at 295K, planar slip is the predominant deformation mode (see Fig. 6b). In contrast, at 77K, the dislocations are tangled into cell walls and hence more uniformly distributed (see Fig. 6a). In fact, there is no obvious evidence of planar slip at 77K. Similar observations were found for an Al-Li-Cu-Mg-Zr alloy [20], i.e. this

alloy showed strong planar slip at room temperature while it deformed more uniformly and had no localized slip bands at 77K.

In general, planar slip will lead to lower ductility since slip bands (micro-bands) may interact with grain boundaries as observed in Fig. 6b. It is well known that there are two ways for dislocations to pass through hardening precipitates, i.e. shearing or bypassing. In previous works [21-25], the authors pointed out that low ductility for precipitation hardening alloys was due to intense, localized deformation. This is result of the promotion of planar slip by coherent, shearable precipitates, and the presence of precipitate free zones (PFZs) at grain boundaries. The present study shows that the reduction of macroscopic ductility could be understood by the fact that moving dislocations are able to shear the coherent and spherical β" (Mg_2Si) precipitates rather than by-passing them. This can be exemplified by the inset picture in Fig. 6b, where a β" precipitate was sheared along the length of the band into two parts, e.g. is similar to that found by Khireddine *et al* [26]. The latter authors reported that at high applied plastic strain, the shearing process of δ' precipitates induces a localization of slip in an aluminum-lithium alloy, leading to an extreme inhomogeneous slip distribution.

From the experimental results described above, it would be expected that the ductility at 295K should be less than at 77K for the present AA6082-T6 alloy. The lower ductility can be explained in terms of the increased tendency for inhomogeneous slip. Further, a high stress concentration arises from localization of plastic deformation in very narrow slip bands, hence favoring microstructure damage evidenced by β" precipitates cut by moving dislocations. However, the improvement in ductility at 77K is considered to be the result of an increase in antiphase boundary energy of β" precipitates at cryogenic temperatures, e.g. see [27]. As a consequence the cutting of β" precipitates by dislocations becomes more difficult. This could in turn partly disperse slip and stimulate for more uniform deformation instead of extensive planar slip. The transition from well-defined intense planar slip at 295K to a more

homogeneous and dispersed slip mode for peak-aged specimens at 77K, cause higher ductility, e.g. as show in Fig. 5.

SEM observations of fracture surfaces were conducted in order to understand the influence of test temperature on fracture mechanisms. As shown in Fig. 7a and b, a large number of dimples associated with considerable plastic deformation were observed at both 77K and 295K. However, obvious differences in the characteristics of the surfaces were evident, e.g. as to the dimple size. As indicated by Fig. 7a, the dimples formed at 77K have a relatively small size, i.e. ~ 0.8μm in average; while at 295K the average dimple size is increased to ~1.2μm. As the dimple size decreases, the number of dimples followingly increases at cryogenic temperature. It is well accepted that dislocation substructures destabilize before fracture and that this is caused by intensive flow localization in relative soft areas. Subsequently, this lead to nucleation of microvoids, growth of microvoids, macroscopic necking and finally failure. Therefore, as observed in this study, the enhanced work hardening behavior at low temperature is accompanied by a higher accumulation of dislocations. The latter is believed to create, e.g., (i) fine scaled substructures with dense dislocation boundaries and (ii) high local dislocation densities at quite small particles. Both these features stimulate nucleation of densely distributed microvoids, i.e. voids formed along the rupturing densely spaced sub-boundaries and around small particles, respectively. In other words, this is another reflection of the more homogenous deformation taking place at cryogenic temperature. Contrarily, the dislocation substructures are coarser and the dislocation density around small particles is less due to the lower dislocation accumulation at 295K. Thus a lower density of dimples being larger is observed on the fracture surface at this deformation temperature (see Fig. 7b).

Also, it is worth noting that the fracture surface at 77K exhibits a higher topography than at 295K, e.g. compare Fig. 7c and 7d. The increased topography at low temperature reflects that deformation is characterized by high storage of dislocations, i.e. dislocation glide

becomes more difficult and spreads in the three dimensional volume of the material and extends normal to the plane of fracture (ref. supporting the observed higher ductility at 77K, Fig 5a.). Further, the stress level experienced at 77K at the same strain as in 295K, is higher. This has two major origins, i.e. an increased dislocation density and a higher lattice friction stress (Peierls stress) at low temperature. The enhanced stress level seems to promote delamination along the grain boundaries elongated in the tensile direction, e.g. see the marked slip steps at delaminations in Fig. 7c. In fact, such grain boundary cracks are similar to what has been reported for testing at low temperature of an Al 2090 alloy [28].

3.3 Specimen surface deformation characteristics

In addition to the fractographic investigations, the surface morphologies (side-view) of specimens tensioned to fracture were investigated. Please note that the observed areas are close to fracture, i.e. the deformation mechanisms in this area is considered to be slightly different from throughout the remaining gauge length. This is due to the higher strain prevailing in the near fracture region. Anyway, micro-voids are clearly visible along some grain boundaries of the specimen tensioned at 77K, as shown in Fig. 8a. . The formation of voids were due to incompatibility of the shape change of neighboring grains which results from lack of sufficient independent slip systems in the polycrystalline material [29]. Due to the relative low strength of precipitates free zones (PFZs), transformation of voids to cracks was likely to take place. In fact, generalized plasticity without such cracking is only possible if mechanisms such as cross slip or activation of additional slip systems occur [30], however, these mechanisms are suppressed at cryogenic temperature [31], leading to formation of voids. Besides for micro-voids, another important feature is that the deformed surface structure at 77K appears heterogeneous in nature with some grains exhibiting micro-bands that are oriented at 30° to 45° to the tensile direction, e.g. see Fig. 8b. A corresponding analysis of slip traces within selected grains having micro-bands is given in Fig. 8c, i.e. with purpose of clarifying the

crystallographic orientation dependence between the tensile direction and {111} planes. It is found that the crystal lattice within these grains rotated in such way that one of the {111} slip planes became nearly parallel to the direction of maximum shear, although the orientation of these grains was more or less different. From Fig. 8c, one can see that the grains marked 1-4, have {111} directions ca. 60° - 68° from the tensile direction, e.g. see the dashed circles in the shown pole figures. This indicates that at cryogenic temperature, the occurrence of slip introducing micro-bands is mostly governed by the grain orientation, i.e., a high Schmid factor. This is consistent with a model for the slip band decohesion micro-mechanism for trigging fracture in age hardenable Al-Li alloys proposed in [32]. In this model, the crack plane angle α with an extending slip band at the crack tip, and several microstructural parameters such as slip band spacing d, slip band width w and yield strength σ were involved. The prediction indicated that an angle $\alpha = \sim 68°$ represents a compromise between a highest possible Schmid-factor and lowest fracture energy for a slip band. In fact, this is in very close agreement to the present observation where {111} directions are ca. 60° - 68° from the tensile direction.

For the specimen deformed at 295K, wavy slip bands extend across the elongated grains approximately perpendicular to the tensile axis (see Fig. 9). This indicates that the dislocation activity occurs on multiple slip planes and spreads by accompanying cross slip. This type of deformation is similar to what has been reported for room temperature deformation of Al single crystals , e.g. [33]. Another difference from the deformation characteristics at 77K is that coarse micro-voids and cracks were formed around constituent particles (marked by yellow arrows in Fig. 9). It is reasonable to suggest that formation of these micro-voids and cracks is stimulated by slip localization, i.e. reducing the ductility at 295K.

To further investigate the surface characteristics, AFM observations were carried out on specimens pre-stretched to a fixed strain of 0.1 at both temperatures. A typical image of the surface appearance of a specimen tensioned at 77K is shown in Fig. 10a. Here slip bands within

grains are quite obscure, and in the example shown for a single grain in Fig. 10c, the average spacing of bands was ~0.40 μm and having a small depth ~10 nm. However, at deformation temperature 295K, slip localizes in clear and wide slip bands. Considerable straight slip bands are clearly seen on the surface in this case (see Fig. 10b and d). The latter representative area includes slip bands having an average spacing of ~ 0.60 μm and depth of ~20nm. Both of these values are larger than that at 77K, hence confirming a more localized mode at 295K (as previously documented by TEM, see Fig. 6). In fact, crack propagation along slip bands occurred, as marked by the dashed circle in Fig. 10b. All these observations are indicative of the negative effects of localization in slip bands on mechanical properties [34].

Moreover, the local misorientation distribution (also called the Kernel average misorientation, or KAM) on the surface of samples deformed at both temperatures were imaged (see Fig. 11). Here, a small area of 200×200 μm^2 was selected for analysis in each case. The brightest red regions indicate the largest local misorientation and dark blue, the lowest. From Fig. 11c and d, it can be found that there is a relative small local misorientation spread for the sample deformed at 77K compared to that at 295K. Thus, indicating that multiple glide on numerous lattice planes was promoted at 77K, whereas deformation at room temperature was significantly more localized. In other words, the more homogeneous deformation at cryogenic temperature is in good agreement with the higher ductility of the present alloy at 77K.

3.4 Effect of pre-stretching on the mechanical properties

As discussed above, changes in the microstructure characteristics such as slip distribution and dislocation density, lattice rotations and surface roughness parameters will be induced during deformation at the investigated temperatures (77K and 295K). To determine which characteristic is the most likely predominant factor influencing the mechanical properties of this alloy, an additional investigation, i.e., pre-stretching to 10% at 77K and 295K and subsequent annealing, was conducted. Pre-stretching at different temperatures probably

induced slightly different amounts of crystal rotations and dislocation densities. The former should be maintained during annealing, while the latter probably recovered to a lower level after long-time annealing. Fig. 12 gives the corresponding room temperature engineering stress-strain curves of specimens pre-stretched at liquid nitrogen temperature (PSL) and at room temperature (PSR) together with the curves representing specimens tested after pre-stretching and annealing (labeled PSLA and PSRA, respectively), the corresponding mechanical properties are listed in Table 2. Especially three observations should be notified:

(1) An apparent yield drop can be found for both the PSL and PSR conditions. This phenomenon is characteristically different from the smooth elastic-plastic transition for the samples with no pre-stretching (see Fig. 5). The PSL condition had a yield drop of ~4.5MPa (constituting about 1.2%) while the PSR had a yield drop of 7.1MPa (~ 1.9%). However, for the conditions containing a subsequent low temperature annealing treatment, i.e., PSLA and PSRA, the yield drops were much less pronounced.

(2) Both the PSL and PSR conditions showed strain softening upon deformation beyond the yield point drop zone at room temperature. However, the corresponding samples subjected to annealing after pre-stretching (PSLA and PSRA), had a normal development consisting of hardening up to maximum strength and then a smooth transition into necking characterized by a significant post-uniform deformation.

(3) The PSL condition exhibited a higher yield strength, ultimate tensile strength as well as larger ductility in comparison with that pre-stretched at 295K (PSR). Similarly, the PSLA condition had higher strength values and higher ductility in comparison with that of the PSRA.

Please also note that the observed yield drop zones for both PSR and PSL specimens in Fig. 12 were reproducible (verified by testing 3 parallels for each condition). One suggests that the occurrence of the peak stress associated with the yield drop zones after pre-stretching (and subsequent room temperature storage for 5 days), is related to (1) dislocation interactions such

as back-stress originated from dislocations pinned at the precipitates dominated by coherent β'' but also constituted by a smaller amount of semi-coherent β' and (2) the fact that a shortage of mobile dislocations probably existed after recovery events occurring upon room temperature storage [35]. Followingly a slightly higher stress was needed to activate plastic yielding, i.e. observed as a peak stress. Once yielding starts, stored dislocations escape from the pinning areas, the stress required to move mobile dislocations decreases and the yield stress starts to drop as also new dislocations are generated. Further, the slip distributions of the pre-strained materials were dependent on the corresponding deformation temperature, i.e. being 77K and 295K respectively. The former having a more homogeneous distribution than the latter condition (see Fig. 6). In other words, after pre-straining at 295K, the established slip bands represent heavily strain-localized zones where the β'' precipitates were sheared into smaller units by the dislocations and hence representing less effective barriers to new interacting dislocations. This in turn also stimulates rapid softening from the peak stress (see Fig. 10b). Upon further deformation, the dislocation density builds up in the localized bands and the stress-strain curve showed an intermediate steady state governed by a balance between localization softening and dislocation hardening. Thereafter, localization softening dominates over hardening and the curve gradually drops towards final fracture. However, after pre-straining at 77K the material, who had a more homogeneous distribution, i.e., less localized slip, develops a much more moderate softening from the peak stress as slip bands get localized, leading to slightly larger ductility to fracture. Here, the intermediate steady state became very short since localized softening spreads and intensifies more and more among activated slip systems and the curve thereby continuously drops towards fracture.

Furthermore, subsequent annealing at 160 °C/5h of the pre-strained conditions showed less yield drop and normal tensile flow curve behaviors (see Fig. 12a). The lower flow stress after annealing (PSLA, PSRA) as compared to the pre-strained states (PSL, PSR) is generally

due to dislocation recovery. In fact, the yield stress after annealing was approximately the same as for the tensile curve conducted at 295K (compare Table 1 and Table 2). A careful examination of the curves in Fig. 12b reveals that the PSLA had a slightly higher flow stress than the PSRA and at the same time larger uniform strain and elongation to fracture (see Fig. 12a). These distinct differences are probably due to the fact that pre-straining at 77K gives higher residual stresses (higher dislocation densities) than for pre-straining at 295K. Hence, upon subsequent annealing at 160 °C, the transformation of β'' to semi-coherent β' becomes more rapid for the PSLA than the PSRA condition [36, 37]. Consequently, slip localization and softening for the PSLA is significantly less pronounced than for the PSRA condition, where the later (PSRA) have relatively more of the shear-able and slip localizing β'' phase. This in turn can therefore explain why the PSLA showed larger uniform elongation and strain to fracture than the PSRA condition (Fig. 10).

It is well accepted that for polycrystalline materials, grains rotate towards more stable orientations with increasing plastic deformation [13]. For FCC materials, uniaxial tensile deformation results in the development of a <111> and <100> double fiber texture parallel to the loading axis, and the relative volume faction of the two fibers generally depends on the deformation temperature [13, 38]. The actual textures of the present four conditions are shown as inverse pole figures (Fig. 13 a-d). As can be seen, all four conditions have a very similar <100> - and a displaced <111> texture. However, the <100> intensity is slightly higher for the room temperature PSR/PSRA conditions than for the PSL/PSLA being subjected to pre-straining at 77K, e.g. intensities 8,6 /8,5 and 7,6/7.8 respectively. One can also note that annealing at 160 °C, did not change the texture intensities (compare PSL versus PSLA, and PSR versus PSRA). The textures are quite similar and have their maximum intensities located relatively far from the orientations giving the highest Schmid factors (see Fig. 13e). Hence, all these conditions would from the grain orientation distribution point of view, experience

activation of multiple slip systems and their tensile curves and mechanical properties should be quite similar. However, the evident <100> texture might partly explain the homogeneous slip and localized slip occurring at 77K and 295K, respectively. According to the deformation study of 99% purity aluminum single crystals [39], the latter authors observed that tensile straining along the <100> direction at 77K exhibited fine multiple homogeneous slip, while at 293K slip was coarse, localized and accompanied by cross-slip. They also investigated the tensile behavior in the <100> direction after pre-deformation, i.e. pre-straining at 77K followed by tensile deformation at 293K. The latter stress-strain curve showed a clear yield drop followed by a steady-state region and ascribed the softening to clustered slip (i.e. localized slip) accompanied by prominent cross-slip. In other words, their results and suggested mechanisms for softening (yield drop zone) and slip distribution mechanisms versus deformation temperature are fully consistent with the present results and associated interpretations of mechanisms described above for the commercial AA6082 alloy.

4 Conclusions

The mechanical behavior of an AA6082 aluminum alloy in the T6 temper condition was investigated using tensile tests at 77K and 295K. The associated characterization of microstructure, texture and engagement of various deformation studies were related to the observed mechanical behaviors. Hence, consistent descriptions of the operating mechanisms behind dissimilar mechanical behavior and phenomena were made.

(1) The mechanical properties, i.e., yield strength, ultimate tensile strength and ductility, improved significantly at 77K in comparison with that obtained at 295K. In general, higher work hardening accompanied by a more homogeneous slip mode can explain the enhanced properties at cryogenic temperature.

(2) Both the PSR and PSL conditions showed a yield point followed by a yield drop zone. The yield drop zone originated from dislocation back stress and shortage of mobile dislocations.

(3) The shape of the yield drop zone depended on the dislocation structure established upon pre-stretching. After pre-stretching at 77 K, slip was quite homogeneous. The subsequent room temperature yield drop developed gradually as the slip process transformed from homogeneous to localized slip in bands. For the counterpart, pre-stretching at 295 K introduced strain localized bands, which immediately caused softening when they re-engaged in the subsequent straining process.

(4) The pre-stretched and annealed conditions showed reduced stress levels, much less pronounced yield point behaviour and improved ductility. Again, pre-stretching at 77 K and annealing demonstrated the highest ductility and work hardening ability, i.e., due to less strain localization and a higher β'/β'' ratio than for the condition pre-strained at 295 K.

Acknowledgments

Financial support from NTNU, Norwegian University of Science and Technology (Program for Joint Research Centers between Norway and China, Grant Pnr. 81730200) is gratefully acknowledged. Zebing Xu also thanks Mr. pål Skaret for assisting during tensile experiments and Dr. Trond Furu at Hydro Aluminum for providing the experimental material.

Reference

[1] R. Borrelly, Merle, P. & Adenis, A., Light Metals 1989; 703-712.
[2] S. Spigarelli, E. Evangelista, H. McQueen, Scripta Materialia, 49 (2003) 179-183.
[3] M.S. Mohamed, A.D. Foster, J. Lin, D.S. Balint, T.A. Dean, International Journal of Machine Tools and Manufacture, 53 (2012) 27-38.
[4] A. Loukus, G. Subhash, M. Imaninejad, Journal of materials science, 39 (2004) 6561-6569.

[5] C. Poletti, M. Rodriguez-Hortalá, M. Hauser, C. Sommitsch, Materials Science and Engineering: A, 528 (2011) 2423-2430.
[6] O. Myhr, Ø. Grong, S. Andersen, Acta Materialia, 49 (2001) 65-75.
[7] C.D. Marioara, S.J. Andersen, J. Jansen, H.W. Zandbergen, Acta Materialia, 49 (2001) 321-328.
[8] G. Buffa, L. Fratini, M. Piacentini, in: Key Engineering Materials, Trans Tech Publ, 2007, pp. 767-774.
[9] R. Kelsey, G. Nordmark, J. Clark, Fatigue crack growth in aluminum alloy 5083-0 thick plate and welds for liquefied natural gas tanks, in: Fatigue and Fracture Toughness—Cryogenic Behavior, ASTM International, 1974.
[10] D.-Y. Park, M. Niewczas, Materials Science and Engineering: A, 491 (2008) 88-102.
[11] I. Braude, T. Grigorova, N. Isaev, V. Pustovalov, V. Fomenko, Low Temperature Physics, 26 (2000) 529-533.
[12] D. Chu, J.W. Morris Jr, Acta Materialia, 44 (1996) 2599-2610.
[13] D.-Y. Park, M. Niewczas, Materials Science and Engineering: A, 497 (2008) 65-73.
[14] J. Polák, J. Man, K. Obrtlík, International Journal of Fatigue, 25 (2003) 1027-1036.
[15] A.K. Gupta, D.J. Lloyd, S.A. Court, Materials Science and Engineering: A, 301 (2001) 140-146.
[16] X. Huang, K. Suzuki, Y. Chino, Journal of Alloys and Compounds, 509 (2011) 4854-4860.
[17] J. Zhou, J. Duszczyk, B. Korevaar, Journal of materials science, 26 (1991) 824-834.
[18] C. Watanabe, R. Monzen, K. Tazaki, International Journal of Fatigue, 30 (2008) 635-641.
[19] T.F. Morgeneyer, M.J. Starink, S.C. Wang, I. Sinclair, Acta Materialia, 56 (2008) 2872-2884.
[20] K.J. Park, C.S. Lee, Scripta Materialia, 34 (1996) 215-220.
[21] J. Lendvai, H.J. Gudladt, V. Gerold, Scripta Metallurgica, 22 (1988) 1755-1760.
[22] J.T.M. De Hosson, A. Huis in't Veld, H. Tamler, O. Kanert, Acta Metallurgica, 32 (1984) 1205-1215.
[23] R.E. Crooks, E.A. Kenik, E.A. Starke Jr, Scripta Metallurgica, 17 (1983) 643-647.
[24] J. Glazer, J.W. Morris, Philosophical Magazine A, 56 (1987) 507-515.
[25] T.H. Sanders Jr, E.A. Starke Jr, Acta Metallurgica, 30 (1982) 927-939.
[26] D. Khireddine, R. Rahouadj, M. Clavel, Acta Metallurgica, 37 (1989) 191-201.
[27] A. Korner, G. Schoeck, Philosophical Magazine A, 61 (1990) 909-915.
[28] K.T. Venkateswara Rao, H.F. Hayashigatani, W. Yu, R.O. Ritchie, Scripta Metallurgica, 22 (1988) 93-98.
[29] A. Ball, R. Smallman, Acta Metallurgica, 14 (1966) 1349-1355.
[30] R. Bowman, R. Noebe, S. Raj, I. Locci, Metallurgical Transactions A, 23 (1992) 1493-1508.
[31] Y. Wang, E. Ma, Applied physics letters, 83 (2003) 3165-3167.
[32] H.J. Roven, Scripta Metallurgica et Materialia, 26 (1992) 1383-1388.
[33] D.E. Kramer, M.F. Savage, L.E. Levine, Acta Materialia, 53 (2005) 4655-4664.
[34] L.Z. He, Q. Zheng, X.F. Sun, G.C. Hou, H.R. Guan, Z.Q. Hu, Materials Science and Engineering: A, 380 (2004) 340-348.
[35] W.G. Johnston, Journal of Applied Physics, 33 (1962) 2716-2730.
[36] S.K. Panigrahi, R. Jayaganthan, in: Materials Science Forum, Trans Tech Publ, 2008, pp. 734-740.
[37] S.K. Panigrahi, R. Jayaganthan, Materials Science and Engineering: A, 492 (2008) 300-305.
[38] C. Taylor, T. Zhai, A. Wilkinson, J. Martin, Journal of microscopy, 195 (1999) 239-247.
[39] S. Miura, K. Hamashima, Journal of materials science, 15 (1980) 2550-2558.
[40] D. Barbier, N. Gey, N. Bozzolo, S. Allain, M. Humbert, Journal of microscopy, 235 (2009) 67-78.
[41] G. Zhu, X. Hu, J. Kang, R.K. Mishra, D.S. Wilkinson, Materials Science and Engineering: A, 528 (2011) 4187-4198.

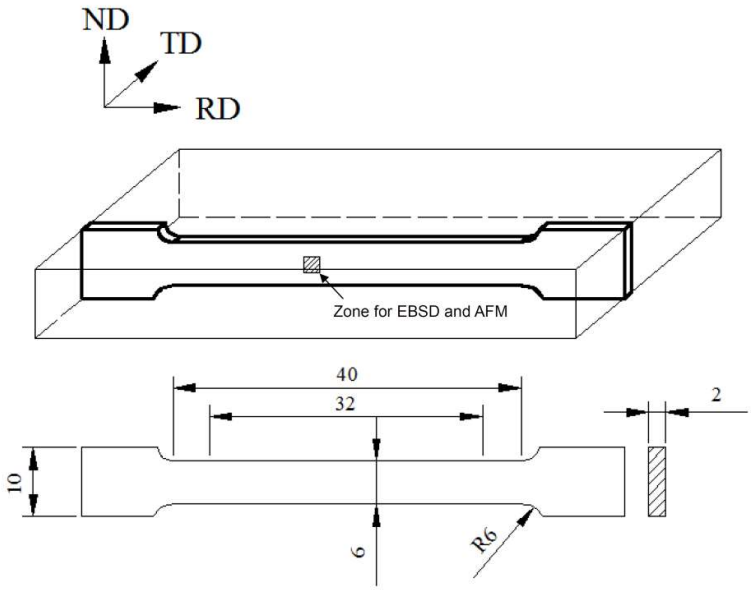

Fig.1. Schematic illustration of the tensile specimen sampling position, actual inspection plane for SEM-EBSD and AFM analysis and dimensions of the tensile test sample [mm].

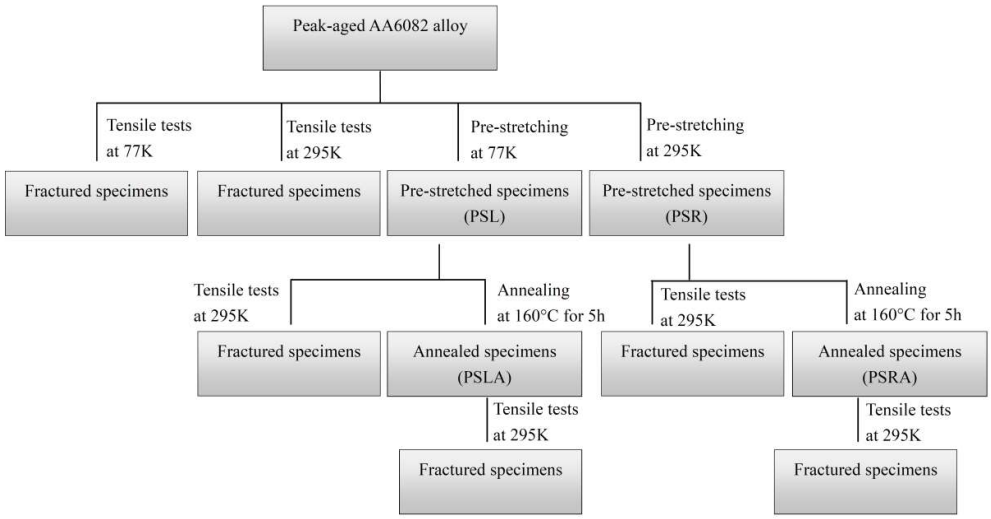

Fig. 2. Process flow sheet for the experimental procedures of the AA6082 alloy.

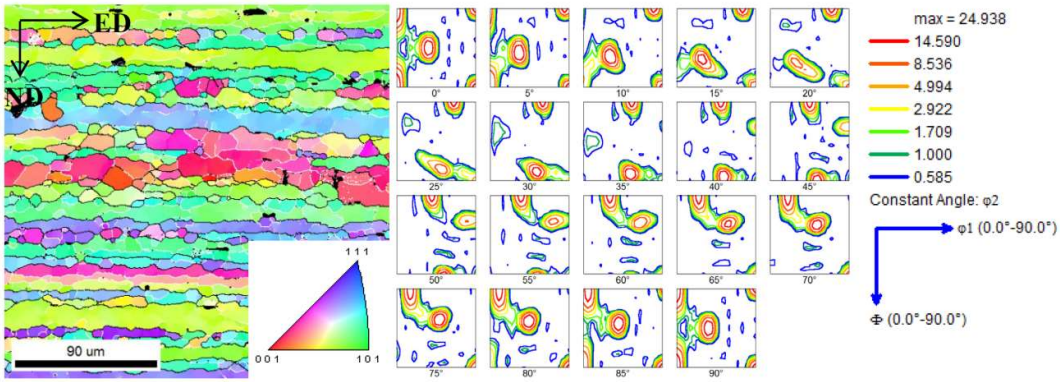

Fig. 3. Grain structure elongated in the extrusion direction (EBSD orientation mapping, TD-plane) and the associated orientation distribution function (ODF) maps for the present peak-aged AA6082 alloy.

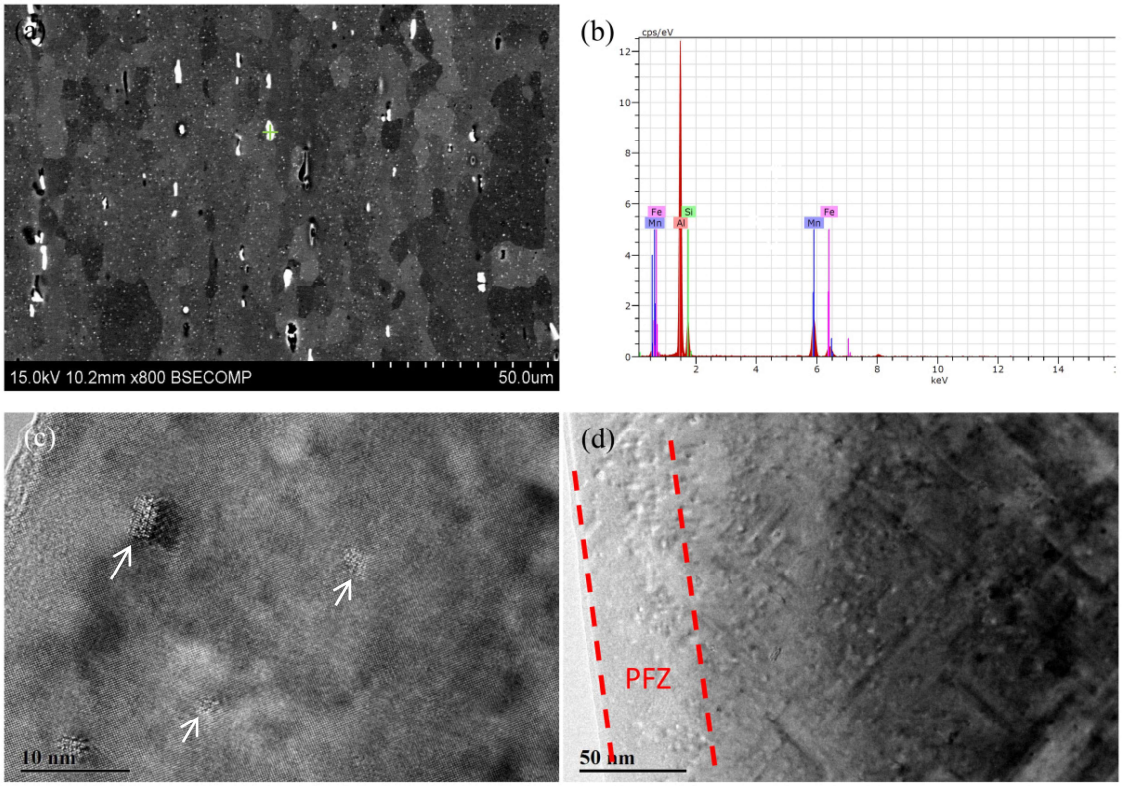

Fig. 4.As extruded and subsequently peak aged alloy AA6082: (a) SEM-BSE image in the TD plane. Primary constituent particles (white contrast) mainly composed of Al, Fe, Mn and

Si, as shown by the corresponding EDS map in (b); (c) TEM high resolution image along the [001] zone axis showing the edge-on morphology of Mg_2Si precipitates, as marked by arrows and (d) typical precipitate free zone (PFZ) along a grain boundary.

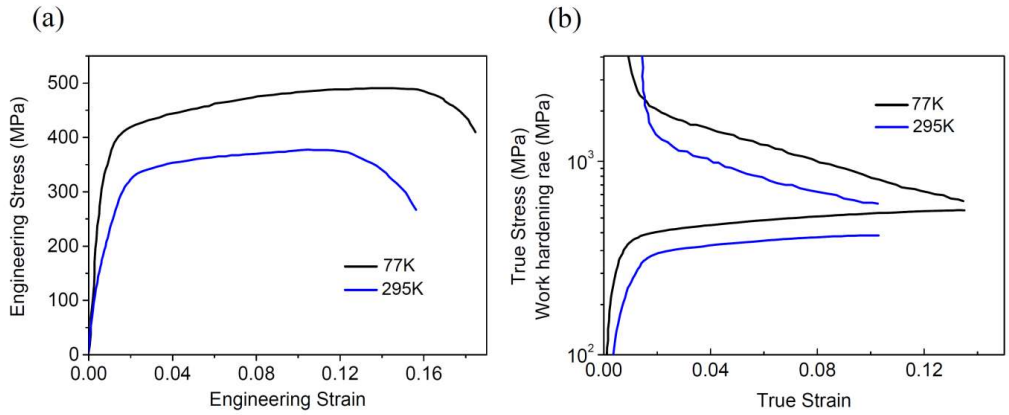

Fig. 5. (a) Engineering stress-strain curves of AA6082 (peak aged) tensioned at 77K and 295K; (b) the corresponding true stress – true strain curves and work hardening rate ($d\sigma/d\varepsilon$) as function of true strain at 77K and 295K. Note, the true stress and work hardening rate (both plotted on the vertical axis) are given in the same units.

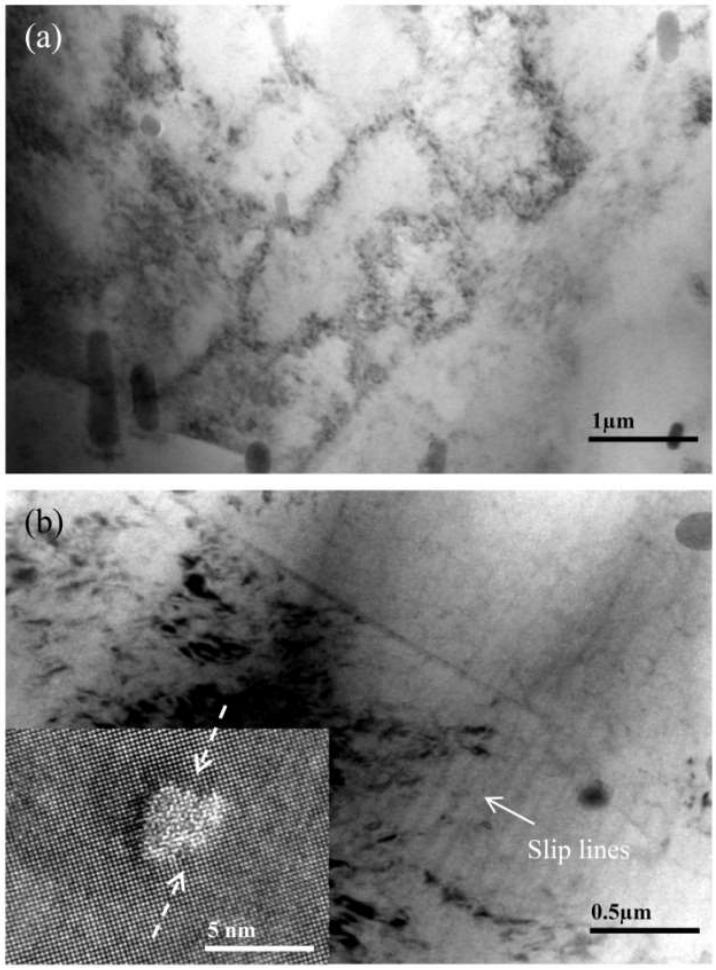

Fig. 6. TEM micrographs of the peak aged AA6082 strained in tension showing (a) homogeneous distribution of deformation at 77K and (b) inhomogeneous planar slip at 295K as pointed out for the parallel 'slip lines'. The insert HRTEM micrograph shows a sheared precipitate. The specimens were deformed to fracture at both test temperatures. Please note that the observed areas were taken from uniformly deformed sections of the specimens.

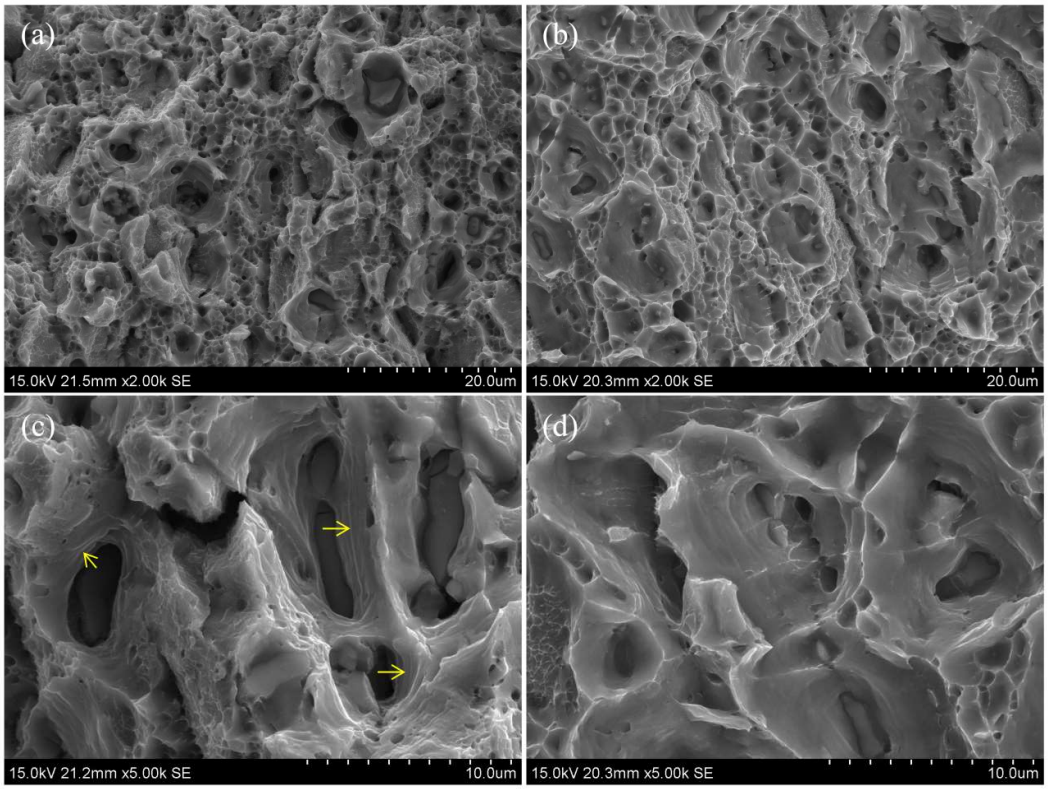

Fig. 7. Tensile fracture surfaces of peak aged AA6082 specimens. (a) and (c) 77K, (b) and (d) 295K. Please note the rougher surface in (c) than in (d). The arrows in (c) indicate slip steps along delaminated boundaries caused by the high stress level.

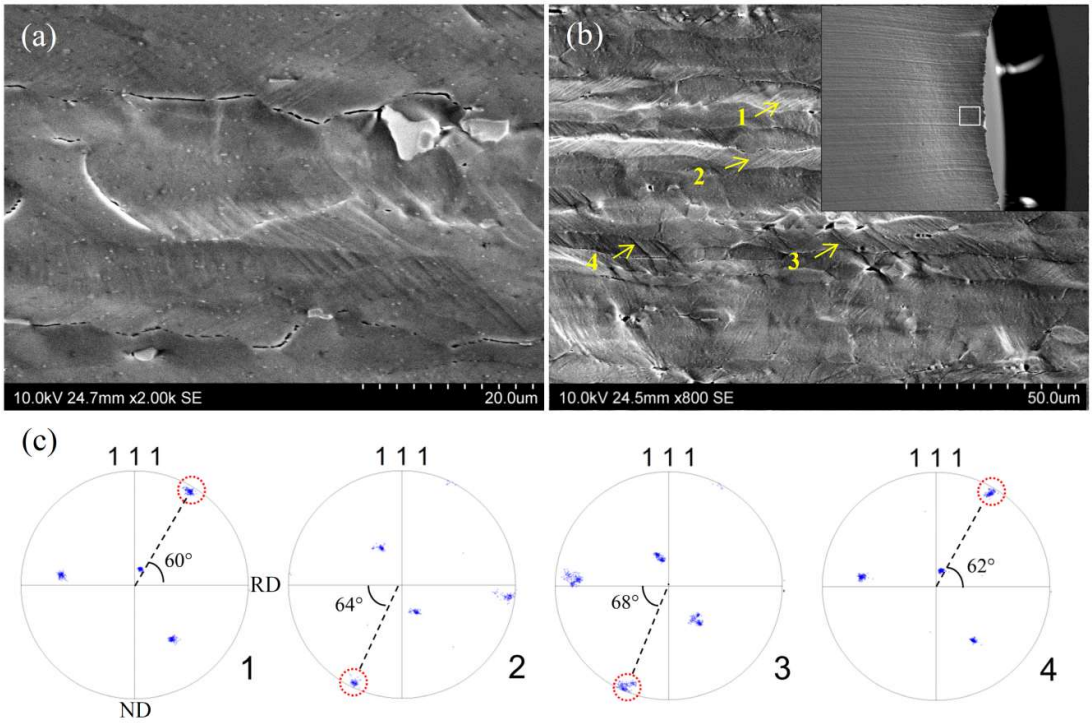

Fig.8. Magnified SEM-SE images of tensile specimen surface (side-view of peak aged AA6082. (a) Cracked grain boundaries containing voids along grain boundaries and smooth roughness slip bands at some distance from the fracture region, 77K; (b) Occurrence of slip bands close to fracture at 77K, i.e. image was taken from the position indicated by the inset; (c) {111} pole figures correspondingly marked for grains 1-4 in (b).The red dashed circles mark poles of important {111} planes and their respective angles to the tensile direction are indicated.

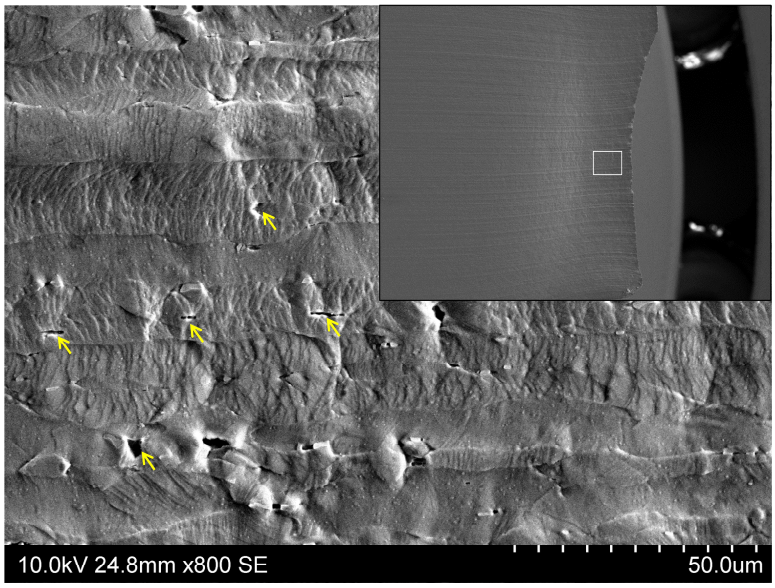

Fig. 9. SEM-SE image surface (side-view) observation in a zone close to fracture after tensile testing at 295K, i.e., taken from the position indicated by the inset. The yellow arrows indicate cracks around constituent particles. Please note that most of the grains appear with roughened wavy slip, whereas some grain surfaces remain more smooth and contour-less.

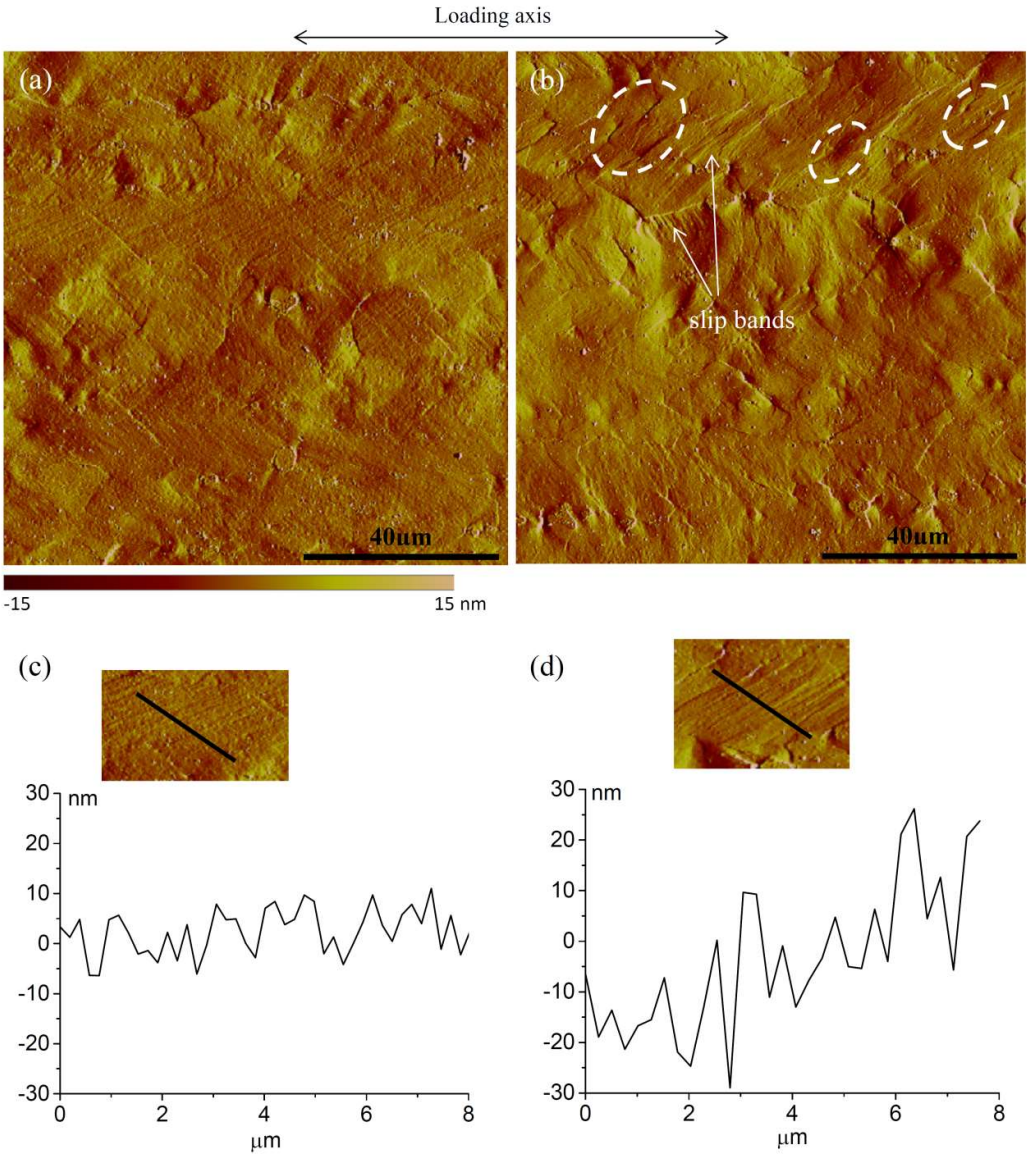

Fig. 10. (a, b) AFM images and (c, d) line scans showing surface slip roughness characteristics of the peak aged AA6082 alloy tensioned to a fixed strain of 0.1 at (a, c) 77K and (b, d) 295K. The arrow at the top indicates the loading axis. Please note the less roughened surface slip topography at 77K (left figures) as compared to the deformation characteristics observed at 295K(right figures). The latter surface contains cracks (dashed ellipse) and clear slip band topography (see arrows in b).

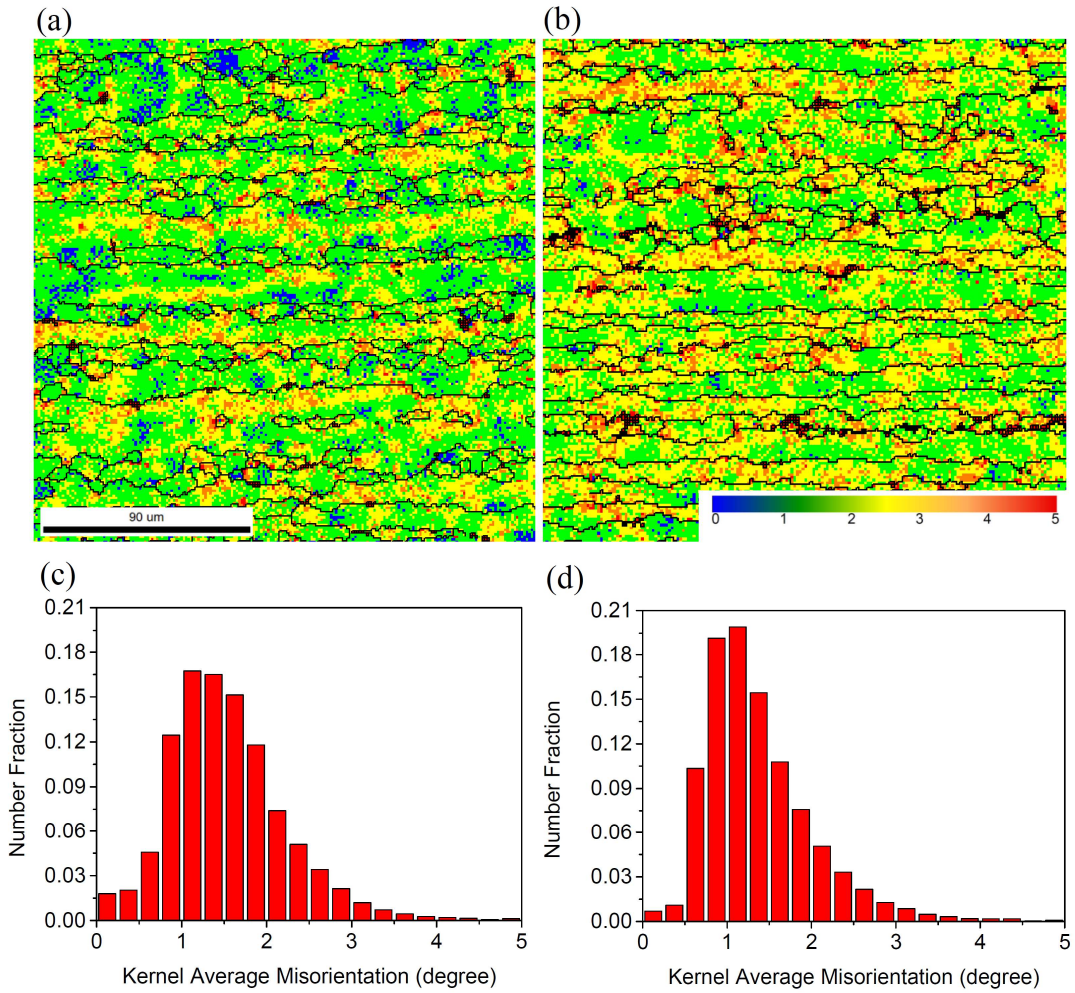

Fig. 11. Kernel (KAM) maps showing the local misorientation gradients on the surface of peak aged AA6082 specimens tensioned to a fixed strain of 0.1 at (a) 77K and (b) 295K. Histograms in (c) and (d) show grain orientation misorientation frequency distributions corresponding to (a) and (b), respectively. Please note that the color scale bar in (b) indicates the level of misorientation, i.e. blue/green and orange/red indicate low and high misorientation gradients, respectively.

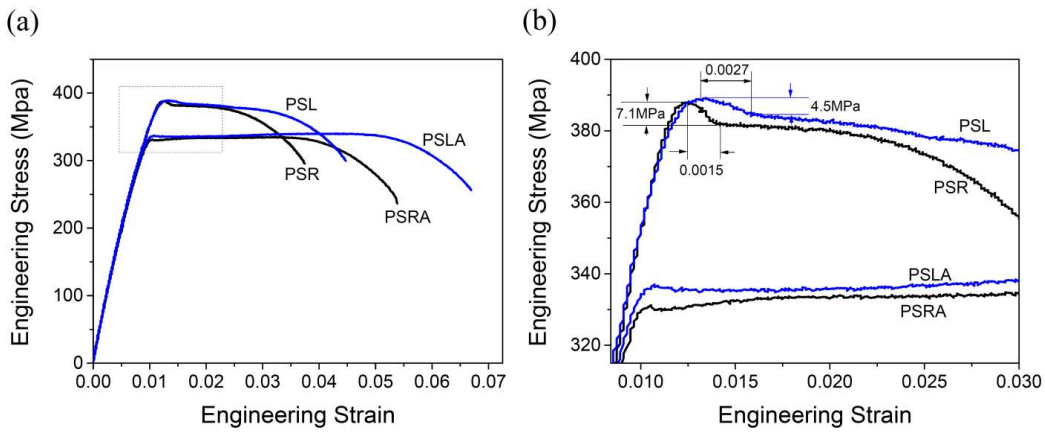

Fig. 12. Engineering stress-strain curves for various conditions of peak aged AA6082 specimens tensioned to fracture at room temperature; (b) magnified sections of the curves indicated by the dashed frame in (a). PSL - prestrained at 77K, PSLA - prestrained at 77K and subsequently annealed, PSR - prestrained at 295K and PSRA - prestrained at 295K and subsequently annealed.

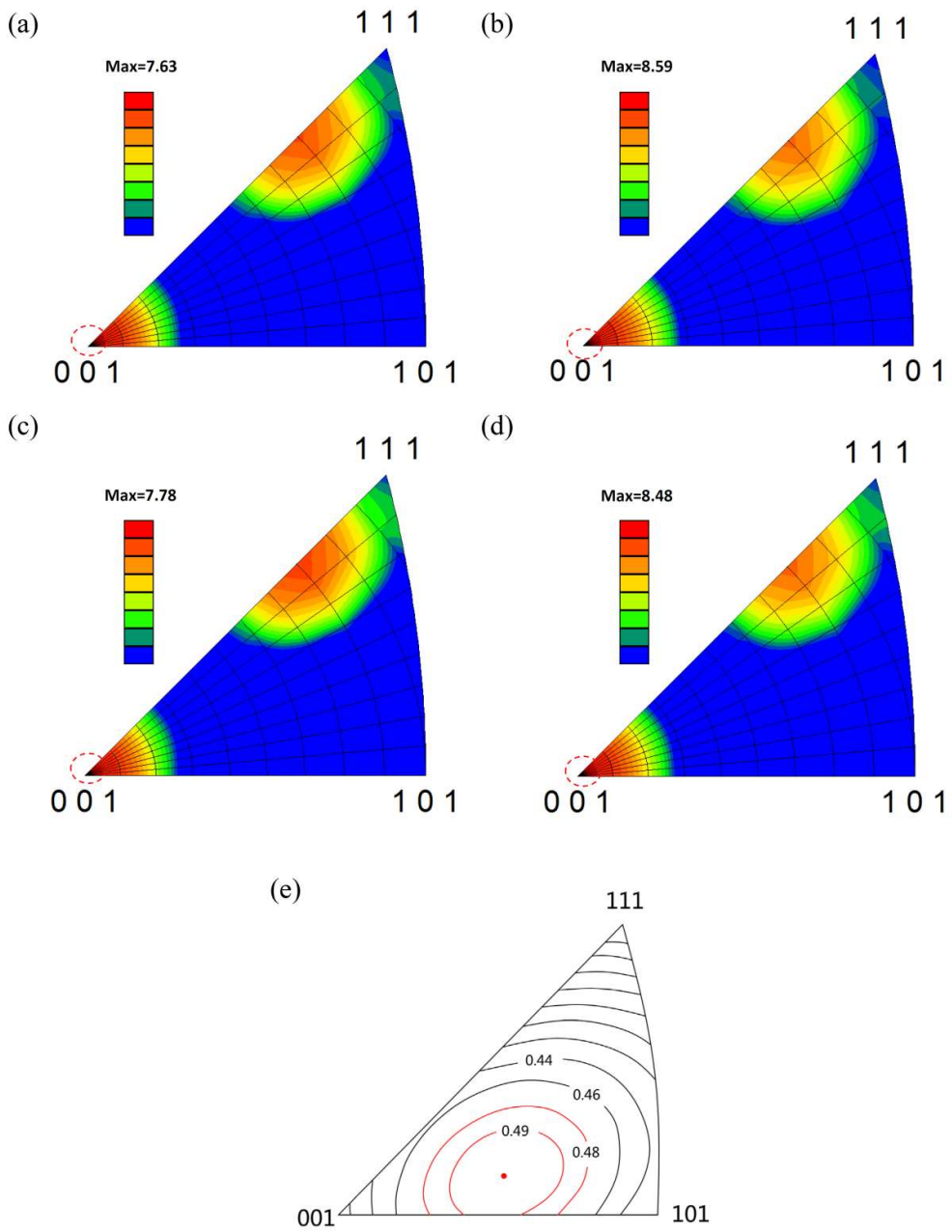

Fig. 13. Effect of deformation temperature on intensity of (001) peaks parallel to the tensile axis of (a) PSL, (b) PSR, (c) PSLA, (d) PSRA, sample conditions. (e) Iso-density lines of maximun Schmid factors plotted in the corresponding unit triangle [40, 41].

Table 1. Tensile properties of peakaged AA6082 at 77K and 295K.

Temperature (K)	Yield strength (MPa)	Ultimate strength (MPa)	Uniform elongation (%)
77	403±10	492±7	15.5±2.6
295	326±8	377±11	11.6±1.9

Table 2. Mechanical properties at room temperature of various conditions of peak-aged AA6082.

Sample	Yield strength (MPa)	Ultimate strength (MPa)	Elongation to failure (%)
PSL	394±6	-	4.5±1.4
PSR	388±5	-	3.7±1.9
PSLA	337±8	340±11	6.7±2.1
PSRA	331±9	334±14	5.4±1.1